

SingleStep 3D Printing of SilverPatterned Polymeric Devices for Bacteria Proliferation Control

*Original*

SingleStep 3D Printing of SilverPatterned Polymeric Devices for Bacteria Proliferation Control / Flores, Gustavo Adolfo González; Bertana, Valentina; Chiappone, Annalisa; Roppolo, Ignazio; Scaltrito, Luciano; Marasso, Simone Luigi; Cocuzza, Matteo; Massaglia, Giulia; Quaglio, Marzia; Pirri, Candido Fabrizio; Ferrero, Sergio. - In: MACROMOLECULAR MATERIALS AND ENGINEERING. - ISSN 1438-7492. - ELETTRONICO. - 307:1(2022). [10.1002/mame.202100596]

*Availability:*

This version is available at: 11583/2932040 since: 2021-10-15T17:17:28Z

*Publisher:*

Wiley

*Published*

DOI:10.1002/mame.202100596

*Terms of use:*

This article is made available under terms and conditions as specified in the corresponding bibliographic description in the repository

*Publisher copyright*

(Article begins on next page)

# Single-Step 3D Printing of Silver-Patterned Polymeric Devices for Bacteria Proliferation Control

Gustavo Adolfo González Flores, Valentina Bertana,\* Annalisa Chiappone, Ignazio Roppolo, Luciano Scaltrito, Simone Luigi Marasso, Matteo Cocuzza, Giulia Massaglia, Marzia Quaglio, Candido Fabrizio Pirri, and Sergio Ferrero

This work describes the fabrication of silver-patterned polymeric devices via light-based 3D printing methods from a tailored resin. An acrylate resin containing silver nitrate ( $\text{AgNO}_3$ ) as a silver precursor is employed to generate silver nanoparticles (AgNPs) through the in situ reduction of the metallic salt. The silver-based resin is processed through a customized stereolithography SL-3D printing to fabricate structures with silver-patterned surfaces. This customized SL-printer (emitting at 405 nm) offers the possibility of adjusting the machine settings during the printing process allowing for AgNPs to be selectively generated by modifying the laser settings during the 3D printing step. Thus, the resin photopolymerization and the photoinduced formation of AgNPs-based strands can be sequentially achieved during the same printing process with the same light source and using the same printable resin. The fabricated silver-patterned devices exhibit different surface features that might be exploited in systems working in a marine environment to control biofilm proliferation. As a proof-of-concept, the antimicrobial behavior of the silver-based 3D printed device is tested against environmental bacterial mixed communities via UV-vis spectroscopy and evaluating the absorbance change. Further tests, however, would be needed to reinforce the evidence of the bacteria behavior on the silver-patterned 3D printed devices.

accurate production of customized objects fabricated on-demand and directly in situ using inexpensive materials.<sup>[1–4]</sup> The flexibility of this technology can be thus strategic, especially when the procurement of disposable materials and small ad-hoc devices is not trivial. 3D Printing allows the fabrication of objects with properties beyond the simple shape dependency. The synergy between material science, machine technology, and object design can enable, in fact, multiple options in a wide range of applications fields, spanning from aerospace to biomedical parts, from building houses to electronic devices and beyond.<sup>[5–10]</sup> 3D Printing includes several different printing techniques that essentially follow the same layer-by-layer building procedure. Among the different types of 3D printing, light-based techniques, such as stereolithography (SL) and digital light processing (DLP), are gaining more attention. Compared to other printing techniques with polymers, such as fused filament formation (FFF) or selective laser sintering (SLS),

the light-based 3D printing techniques combine faster printing rates and higher printing resolution with inexpensive materials and equipment.<sup>[11]</sup> These technologies use liquid resins conveniently modified by combining the desired elements to

## 1. Introduction

The recent global health crisis has demonstrated that 3D printing could be a valuable resource in emergency cases for the fast and

G. A. González Flores, V. Bertana, A. Chiappone, I. Roppolo, L. Scaltrito, S. L. Marasso, M. Cocuzza, G. Massaglia, M. Quaglio, C. F. Pirri, S. Ferrero  
 Department of Applied Science and Technology  
 Politecnico di Torino  
 Corso Duca degli Abruzzi 24, Turin 10129, Italy  
 E-mail: valentina.bertana@polito.it

G. A. González Flores, A. Chiappone, I. Roppolo, G. Massaglia, M. Quaglio, C. F. Pirri  
 Center for Sustainable Future Technologies @PoliTo  
 Istituto Italiano di Tecnologia (IIT)  
 Via Livorno 60, Turin 10144, Italy  
 S. L. Marasso, M. Cocuzza  
 CNR-IMEM  
 Parco Area delle Scienze 37a, Parma 43124, Italy

 The ORCID identification number(s) for the author(s) of this article can be found under <https://doi.org/10.1002/mame.202100596>

© 2021 The Authors. Macromolecular Materials and Engineering published by Wiley-VCH GmbH. This is an open access article under the terms of the Creative Commons Attribution-NonCommercial License, which permits use, distribution and reproduction in any medium, provided the original work is properly cited and is not used for commercial purposes.

DOI: 10.1002/mame.202100596

produce 3D-printed objects with specific properties.<sup>[12–15]</sup> Typically, a 3D printable resin is based on three main components: a) monomers/oligomers, which determine the final physical and mechanical characteristics of the printed structure, b) photoinitiators, which establish the reactivity of the resin during the polymerization reaction and c) a dye or colorant which controls the light penetration during 3D printing (Z-axis) and ensures a high resolution (XY plane).<sup>[16]</sup> Besides, (nano)particles such as graphene oxide, carbon nanotubes, or even cellulose nanocrystals can be added to the resins to enhance the printed part properties.<sup>[17–19]</sup> Nevertheless, nanoparticles' addition into the resin could limit its printability by decreasing the formulation flowability and stability (hence, the resin viscosity increase considerably according to the nanoparticles features),<sup>[20,21]</sup> the light absorption, and ultimately the printing resolution.<sup>[22,23]</sup> A clever approach that can circumvent these problems is to use a filler precursor (e.g., metal-based salts) that allows maintaining good printability and, at the same time, enable the formation of the desired fillers in a second step.<sup>[24–27]</sup>

By combining the right components, 3D printed parts can be applied in specific and subtle fields such as the biomedical one, especially in cases related to preventing problems caused by biofouling.<sup>[28,29]</sup> Biological fouling, commonly denoted as biofouling, refers to the accumulation of unwanted biological matter on surfaces.<sup>[30]</sup> It comprises both biofilms formed by microorganisms and macroscale biofouling (usually called macrofouling) created by macro-organisms. In this view, 3D printed objects designed with practical features could play a fundamental role, for instance, in mitigating the risk of infection associated with bacteria proliferation, increasing the working life of 3D printed medical tools and devices.<sup>[28,31]</sup> However, the interest in antifouling and antibacterial materials goes beyond the medical and biomedical fields, including environmental science, marine science, and a wide range of industrial sectors dealing with food and beverage to mitigate health risks, with environmental and financial consequences.<sup>[30,32]</sup> When it comes to marine applications, the issues range from more conventional complications related to bacterial accumulation (and their derived effects) on ships and offshore platforms to more recent problems associated with the increasing field of blue energy technologies.<sup>[33]</sup> Blue energy comprises all technologies able to harvest renewable energy in oceans, from the well-established offshore wind to emerging technologies such as wave, tidal, current, ocean thermal, osmotic power, biomass production from algae and microbial fuel cells.<sup>[34–36]</sup> In these scenarios, the biofouling effect represents one of the main constraints affecting the overall system performance for energy generation in marine environments.<sup>[37–39]</sup> Thus, implementing materials with suitable antimicrobial activity could help overcome such limitations.

Regarding the strategies to confer antifouling and antimicrobial features to polymeric 3D printed parts, the literature reports numerous approaches using specialized agents such as quaternary ammonium or carboxylic acid groups.<sup>[40–45]</sup> Likewise, antimicrobial components such as tetracycline hydrochloride in a poly( $\epsilon$ -caprolactone)-polyvinyl pyrrolidone (PCL-PVP) blends can be used to produce 3D printed thermoplastic patches with antimicrobial properties.<sup>[46]</sup> The antimicrobial efficiency of 3D printed PCL scaffolds can be enhanced by a multiple-step approach, including the adsorption of poly(lactic-co-glycolic acid),

or PLGA, microspheres loaded with vancomycin components.<sup>[47]</sup> Another suitable strategy is to exploit the well-known antimicrobial properties of silver nanoparticles (AgNPs).<sup>[48]</sup> The antifouling and antimicrobial effect of AgNPs against microorganisms is well-known, and although their bactericidal mechanisms are not entirely understood, the literature reports multiple approaches related to the interaction between silver nanoparticles and bacteria based on the distribution, shape, and size of these metallic nanoparticles.<sup>[49–52]</sup> Good agreement exists considering the antimicrobial behavior of AgNPs to be mainly related to their strong oxidative activity, which is responsible for the release of silver ions.<sup>[53,54]</sup> Microorganisms approaching the AgNPs-reached surfaces are prone to the cytotoxic effects induced by ion adsorption. Indeed, Ag ions can perforate the cell membrane, inducing accumulation on negatively charged parts of the cellular membrane and finally inducing cell death. Hence, the correct configuration and integration of AgNPs within a polymeric substrate could play a fundamental role in effectively interacting with microorganisms.<sup>[55,56]</sup> The incorporation of silver functionalities into a polymer can be via either direct dispersion of silver particles within the polymer matrix,<sup>[57,58]</sup> or exploiting the in situ reduction of a silver precursor (e.g., silver nitrate or silver perchlorate) dispersed in the polymeric medium for obtaining AgNPs through thermal, electrochemical, or photochemical approaches.<sup>[59–61]</sup> Different investigations have reported 3D printed polymer-silver nanocomposites with antibacterial properties.<sup>[62–65]</sup>

This work aims to fabricate silver-patterned structures, with antifouling features, through light-based 3D printing from a photocurable resin containing silver nitrate ( $\text{AgNO}_3$ ) as a silver nanoparticle precursor. Here we propose an innovative technology strategy using light-based 3D printing techniques to manufacture 3D structures with engineered surface design in which only certain areas display antimicrobial properties. By dispersing  $\text{AgNO}_3$  accurately in a suitable photocurable monomer, we prepared a stable and easily printable resin that we processed through a customized SL-3D printer to achieve the sequential polymerization of the resin and the photo-induced in situ reduction of a silver salt. Various works have reported similar approaches where silver salts (e.g., silver acetate or silver nitrate) are directly incorporated into a photocurable formulation for imparting specific properties to the printed parts.<sup>[27,59,66]</sup> Our strategy, however, was to use a customized top-down SL-3D printer with the possibility to change the machine settings during the 3D printing step itself. Indeed, our previous studies focused on the printing of such resin with the aid of bottom-up digital light processing (DLP) technology. Although DLP allows the printing of a whole layer in a single 3D printing step, increasing the building rate, it does not offer the possibility to tune the light intensity within the same printing process. Thus, a UV post-process was required to supply to silver precursors the right energy to precipitate nanoparticles. Furthermore, this process can be activated only on external surfaces with limited spatial control. The customized SL-3D printer used in this work instead allows to scan point by point every layer, triggering local energy fluence. Thus, the AgNPs were selectively generated by changing the laser printer settings, producing silver-based strands during the same 3D printing polymerization step with the same light source. After the selective patterning of the structures, the silver

**Table 1.** Acrylate conversion (%) of PEGDA575 and AgNO<sub>3</sub>-PEGDA575 formulations during real-time FTIR experiments upon visible light irradiation (405 nm) and after the 3D printing and UV postcuring steps. Insoluble fraction (%) calculated on 3D printed samples.

Sample	Acrylate conversion [%]			Insoluble fraction [%] <sup>c)</sup>
	Visible light <sup>a)</sup>	After 3D printing	UV postcured <sup>b)</sup>	
PEGDA575	90	86	89	95
AgNO <sub>3</sub> -PEGDA	84	82	93	89

<sup>a)</sup> The acrylate conversion evolution and the full FTIR spectra of the formulations upon visible light irradiation are shown in Figure S1 (Supporting Information); <sup>b)</sup> 92% is the acrylate conversion of the just 3D printed samples with generated Ag-NPs over its surface and before the UV post-curing. The full FTIR spectra of all the 3D printed samples are shown in Figure S2 (Supporting Information); <sup>c)</sup> Determined on the polymerized samples during the FTIR tests.

precursor excess could be removed in a dedicated post-printing washing step. This process is an alternative to the conventional multimaterial approach since the whole material is fabricated from the same polymeric resin, avoiding adhesion problems, differences in thermal expansion, and compatibility.<sup>[67]</sup> To the best of our knowledge, this is the first study in which 3D printed structures with specific and well-defined silver strands are produced using the same 3D printer machine and from the same material. Finally, the antimicrobial behavior of the silver-patterned 3D printed structure was tested over time against a combined environmental microorganism community through UV-vis spectroscopy evaluating the absorbance change.

## 2. Results and Discussion

Preliminary investigations were focused on evaluating the resin reactivity performance in conditions similar to that of the top-down SL-3D printer, where the resin's upper side always remains in direct and continuous contact with the air. For this purpose, real-time FT-IR measurements were carried out on the photocurable resin based on PEGDA575 monomer containing 15 wt% of silver nitrate (the AgNO<sub>3</sub>-PEGDA resins) and PEGDA575 formulation without silver salt. The acrylic double bond conversion was monitored by following the decrease of the characteristic peak at 1640 cm<sup>-1</sup>. The acrylate conversion curves (Figure S1, Supporting Information) show high conversion values are reached after 10 s of irradiation. In **Table 1**, the acrylate conversion (%) under visible irradiation is reported at the plateau value.

Although the measurements were performed in the air (where oxygen might inhibit the free-radical reaction), the conversion of the AgNO<sub>3</sub>-PEGDA resin was quite high, reaching conversions of 83%, but slightly lower compared to the PEGDA575 formulation. The insoluble fractions of the just polymerized films were also evaluated. The polymerized PEGDA575 films reached a higher gel content (near 95%) compared to the PEGDA575 samples containing silver salt (near 89%), which can be associated with a lower crosslinking density due to the silver salt presence, but also with the amount of silver salt washed out during the test, leading to significant differences in the measurement. These results indicate that the silver salt presence slightly influences the

acrylate reaction; however, the acrylate conversion can increase by supplying higher irradiation doses to the photocurable system (e.g., UV postcuring treatment).<sup>[68–70]</sup> After verifying the formulation reactivity upon visible light irradiation in direct contact with air, we moved toward the 3D printing step using the customized top-down SL-3D printer. This 3D printer offers the possibility to change specific settings during the printing process itself, such as laser intensity, laser velocity, and hatch spacing (namely, the spacing between two consecutive scanned lines). Hence, by setting the appropriate printing parameters, two conversions can be performed in the same process, as represented in **Figure 1a**: i) the resin photopolymerization and ii) the sequential and selective photogeneration of AgNPs.

The initial printing parameters were set based on previous investigations, considering the reported light fluence values applied to polymerize the silver salt-based resin.<sup>[27]</sup> Laser power and hatch speed (strictly related to light fluence) can be changed in a range of 1–120 mW (stepping 1 mW) of laser power and 0.5–2000 mm s<sup>-1</sup> of laser scan speed. Therefore, laser nominal output power of 10 mW, laser scan speed (hatch speed) of 750 mm s<sup>-1</sup>, hatch spacing of 50 μm and layer thickness of 100 μm were selected; the hatch spacing of 50 μm yielded a 30 μm of overlapping between consequent polymerized lines and thus a mechanically stable 100 μm thick polymerized layer. The 3D printed parts resulted in orange-colored due to the RO dye, as shown in **Figure 1b**. Then, the machine settings were changed to provide higher light energy to induce the photoreduction of silver ions embedded in the polymeric matrix.<sup>[71]</sup> Upon adequate light energy absorption, the silver ions (Ag<sup>+</sup>) reach an excited state (Ag<sup>+</sup>) that, in the presence of free radicals or electrons (coming from the photoinitiator, solvent, or other environmental elements), can be reduced to form silver atoms (Ag<sup>0</sup>). Afterward, the nucleation and growth process of silver particles follows.<sup>[72]</sup> Since the Ag-NPs formation is triggered by giving adequate light energy to the system, different fluence parameters were investigated, ranging from 0.08 to 0.38 J mm<sup>-2</sup>. The corresponding SL printer parameters (in terms of laser nominal output power and hatch speed) are reported in **Table 2**.

Among the different considered parameters, those with 30 mW of laser nominal output power and 1 mm s<sup>-1</sup> of laser scan speed (test-5 in **Table 2**) produced the most satisfactory results in terms of silver NPs generation, witnessed by the formation of mirror-like lines in the areas where the laser passed, as shown in **Figure 1c**. This color change reflects the effective generation of AgNPs, which was also confirmed by UV-vis spectroscopy analyses (see **Figure 1d**), showing the characteristic silver surface plasmon resonance (SPR) peak in the visible region.<sup>[71,73]</sup> The film part without AgNPs exhibited a modest shoulder around 400 nm associated with the unreacted BAPO photoinitiator.<sup>[74]</sup> Hence, the parameters chosen for downstream investigations were set at 30 mW of laser nominal output power and 1 mm s<sup>-1</sup> of laser scan speed, obtaining 30 μm wide patterns rich in AgNPs. Acrylate conversion was also investigated in the 3D printed parts. The just 3D-printed PEGDA-AgNO<sub>3</sub> samples reached acrylate conversions of about 82%, slightly lower than the acrylate conversion reached by the PEGDA575 formulation in the same printing conditions (**Table 1**). These measurements are in good agreement with real-time FT-IR measurements. As expected, the samples reached higher acrylate conversions by increasing the light

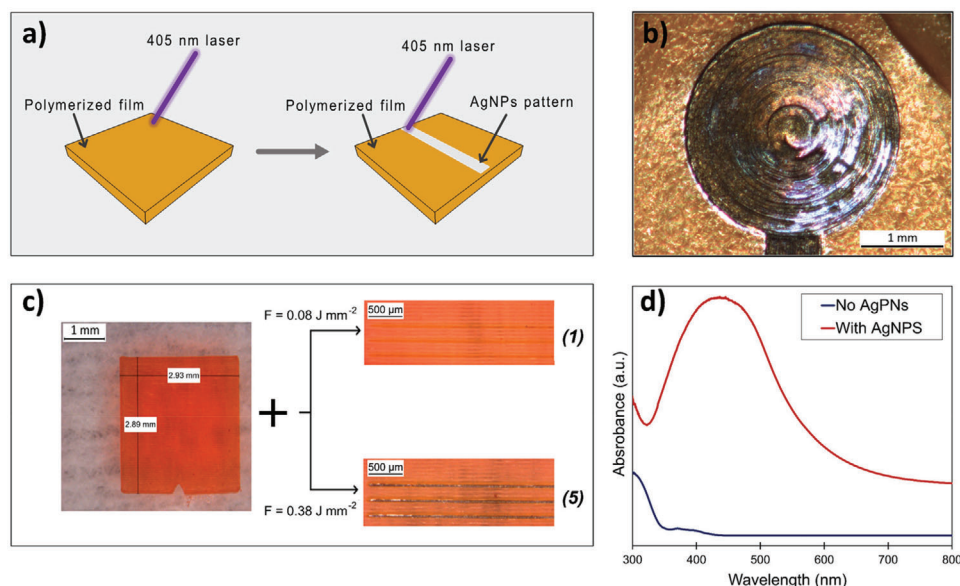


**Figure 1.** Illustration of the overall 3D printing process for creating silver-patterned polymeric devices. a) Representation of the SL-3D printing and selective AgNPs pattern generation using the customized printer. b) Picture of a 3D printed sample with AgNPs patterns created with the optimized parameters. c) Pictures of the 3D printed samples from the 15 wt%  $\text{AgNO}_3$ -PEGDA formulation showing the results obtained during the AgNPs generation step using  $0.08 \text{ J mm}^{-2}$  fluence (test-1) and  $0.38 \text{ J mm}^{-2}$  (test-5); see Table 2 for the complete laser settings and details. d) UV-vis absorbance spectra of polymerized thin films before and after AgNPs formation.

**Table 2.** SL-3D printer parameters investigated for the photogeneration of AgNPs with the customized (405 nm) SL-3D printer.

Test (N°)	Fluence [ $\text{J mm}^{-2}$ ]	Laser power [mW]	Hatch speed [ $\text{mm s}^{-1}$ ]
1	0.08	30	5
2	0.09	30	4
3	0.13	30	3
4	0.19	30	2
5	0.38	30	1

energy dose up to 92% after the AgNPs generation. A complex-shaped 3D printed object was designed and processed to demonstrate the proposed printing process capabilities. **Figure 2a** shows the object CAD design, which has an  $18 \times 18 \text{ mm}^2$  base and is 9 mm high. The smallest features of the object are  $450 \mu\text{m}$  thick tilted inner walls, with empty and void features supported by diagonal beams. The structure was effectively printed, successfully performing the two mentioned steps (see **Figure 2b**). On the demonstrator steps, the acronym of our laboratory, “Chi-Lab,” is written with a controlled generation of AgNPs (**Figure 2c**). This object demonstrates that the selective AgNPs generation could be achieved not only for planar geometries but even on different heights along z-direction in the same printing process. As previously mentioned, the generation process allows obtaining  $\approx 30 \mu\text{m}$  wide AgNPs strands, as reported in **Figure 2d**.

The distribution and size of the generated AgNPs were examined by scanning electron microscopy (FESEM). As detailed in **Figure 3a**, the AgNPs were evenly distributed throughout the surface and are mostly spherical. Besides, it should be noted the high surface density of the generated AgNPs, and in particular, the

large size distribution (**Figure 3b**), ranging from 50 nm to 160 nm roughly. The energy-dispersive X-ray (EDX) analysis showed the atomic concentration of silver on the sample’s surface and the concentration of carbon and oxygen related to the polymeric matrix (**Figure 3c**). Furthermore, as visible in **Figure 3d**, the size and concentration of AgNPs decrease moving from surface to bulk. Such behavior can be attributed to the light penetration in the material, with higher irradiance on the top of the sample. **Figure 3d** shows that the selected parameters allow a nanoparticles-rich region of about  $1 \mu\text{m}$  from the sample surface.

A washing procedure on the printed samples was carried out to remove the unreacted components (monomers, photoinitiators, dye, and silver salt) that can lead to undesired material modification overtime. The procedure was accomplished as follows: once the printing and AgNPs generation processes were completed, the printed parts were rinsed in isopropanol and immersed in deionized water overnight (about 16 h) to remove the unreacted components; the parts were then slowly dried at room temperature. During this washing protocol, the PEGDA575 matrix swells, facilitating the removal of silver salt. XPS analysis was performed to compare different samples and to evaluate the washing protocol. One sample was analyzed as printed (named  $\text{AgNO}_3$  unwashed) while a second one underwent the above-described washing protocol just after the printing ( $\text{AgNO}_3$  washed); these two were furtherly compared with a printed sample that underwent the silver reduction protocol (AgNPs). **Figure 4a** shows the collected survey spectrum from the three samples, where the presence of C and O associated with the polymeric matrix and Ag coming from the silver salt and AgNPs are displayed (see the inset table in **Figure 4a**). First, a considerable decrease in intensity at the Ag peak can be observed in the survey spectra for the washed sample compared to the unwashed



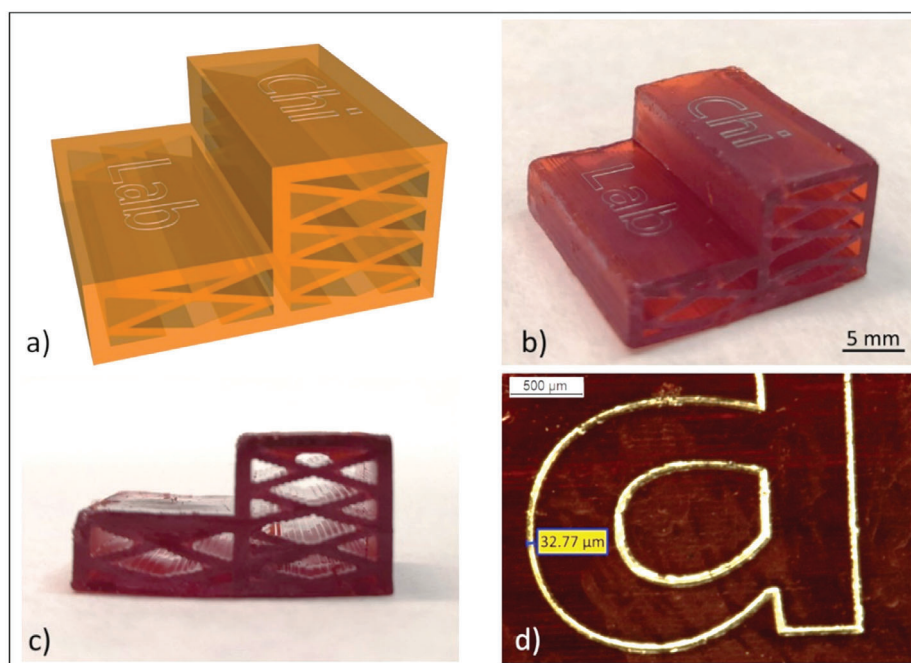


**Figure 2.** The 3D object was built with the  $\text{AgNO}_3$ -PEGDA formulation. a) CAD design ( $18 \times 18 \times 9 \text{ mm}^3$ ). b) The 3D-printed object. c) Lateral view of the object. d) A microscope image with the detail of the letter "a" in the word "Lab."

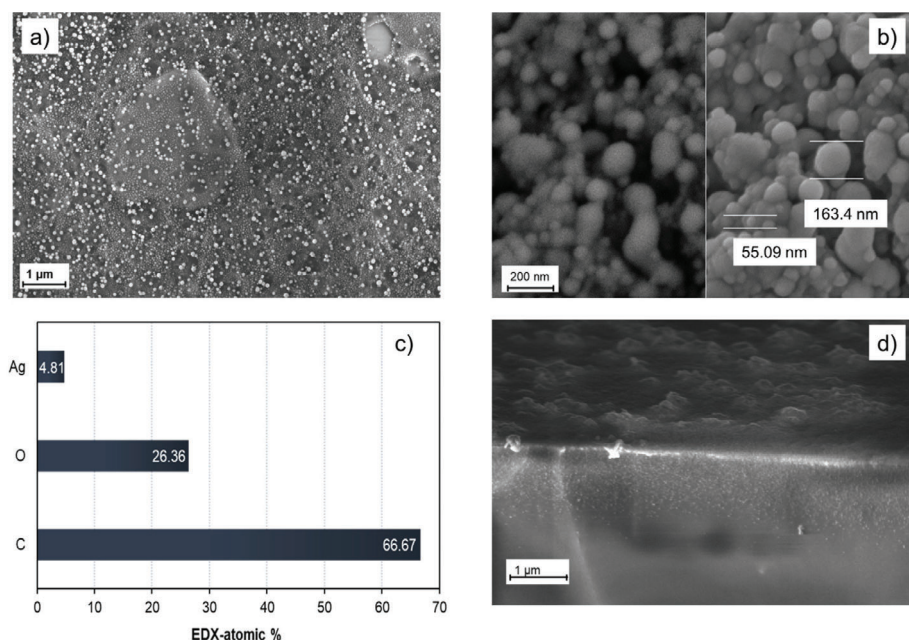


**Figure 3.** FESEM images of the 3D printed samples with generated AgNPs on the sample surface from 15 wt%  $\text{AgNO}_3$ -PEGDA formulation, a,b) top view, c) energy-dispersive X-ray (EDX) results of the sample, and d) 45° view of the sample's cross-section.

sample, with atomic percentages of 0.6% and 4.9%, respectively, indicating the effective removal of silver salt from the samples after the washing step. This observation is better appreciated in Figure 4b, where the high-resolution spectra of double Ag peaks associated with  $\text{Ag}3d_{5/2}$  and  $\text{Ag}3d_{3/2}$  are displayed. The intensity of the silver-associated peaks is significantly lower for the washed sample.

Considering the binding energy value for metallic Ag of 368.2 eV as a reference (corresponding to  $\text{Ag}3d_{5/2}$ ),<sup>[75]</sup> the differences in the binding energy of silver can be appreciated. The values displayed are 366.67 eV for the sample with generated AgNPs and 367.5 eV for the unwashed sample. The  $\text{Ag}3d_{5/2}$  peaks shifting toward lower binding energies of these samples might be associated with the change of oxidation states of silver ions to

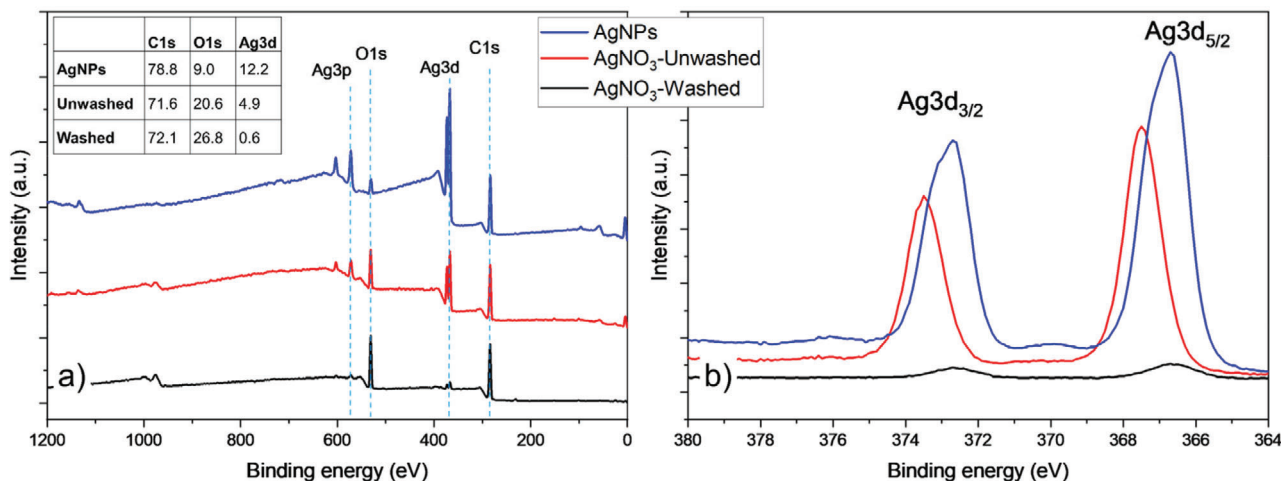


**Figure 4.** a) XPS survey spectra of samples with generated AgNPs (blue line), unwashed sample (red line), and washed sample (black line) 3D printed samples. The inset table displays the atomic percentage % of the three types of printed samples. b) Ag3d double high resolution (HR) XPS spectra of the sample with AgNPs (blue line), unwashed sample (red line), and washed sample (black line). All samples were produced from PEGDA575 formulation containing 15 wt% of silver salt ( $\text{AgNO}_3$ ).

metallic AgNPs ( $\text{Ag}^0$ ),<sup>[71]</sup> even if the formation of  $\text{Ag}_2\text{O}$  on the AgNPs that has a binding energy of 367.8 eV cannot be excluded.<sup>[76]</sup> As the last experiment to characterize the washing protocol effectiveness, the washed samples were subjected to a UV postcuring treatment for 15 minutes. No change in the sample coloration was observed, remaining with a bright-orange aspect, see Figure S3a (Supporting Information). Different coloration result was obtained by not washing the sample previously; in this case, the not-washed sample reaches a brown look aspect after exposing it to 15 min of UV irradiation, see Figure S3b (Supporting Information). Such color indicators evidence the effective removal of silver salt excess during the developed washing protocol, avoiding the uncontrollable and spontaneous generation of AgNPs over time. The water used for the overnight washing procedure of the samples was analyzed by UV-Vis spectroscopy (see Figure S3c, Supporting Information). An absorption shoulder related to the extraction of the reactive orange dye was only visible in the spectrum.<sup>[77]</sup>

The antibacterial properties of the AgNPs-3D-printed objects were tested against environmental bacteria. The antibacterial tests were performed on 3D-printed tabs obtained from the  $\text{AgNO}_3$ -PEGDA formulation with AgNPs generated as described in the Experimental section. Each 3D-printed tab (shown in Figure 5a) was immersed into 10 ml of environmental suspension (1:100 ratio). The bacterial viability was evaluated through UV-vis spectroscopy after 24, 72, and 120 h of incubation; the results are plotted in Figure 5b,c. Samples containing silver nanoparticles showed a reduced absorbance value over time, as observed in Figure 5c, which suggests an increase in the antibacterial effect. The lowest absorbance value was measured at 120 h for samples with a hatch spacing of 20  $\mu\text{m}$  (Figure 5c), hence with the higher density per unit area of AgNPs. After 120 h exposure, the absorbance value is generally characterized by a lower variability (smaller error bars). Such behavior could indicate an antibacterial effect that does not decrease over time. On the contrary, it increases and becomes accurate for longer periods, thus adding sustainability to the device. The bacteria solution containing the

3D-printed tabs without AgNPs on their surface showed an absorbance value at 120 h, almost similar to the solution not containing any 3D printed sample (inoculum) (Figure 5b). The obtained results are in good agreement with the general antimicrobial mechanism of AgNPs, which is a release-based one, being  $\text{Ag}^+$  ions the released species.<sup>[53]</sup> The time dependence of the antibacterial effect can be well explained by the release and subsequent accumulation over time of the  $\text{Ag}^+$  ions inside the microorganisms, up to cell death. These results confirm that the AgNPs in the 3D-printed objects are available for ion release-based antimicrobial processes and that the proposed approach here allows good control of AgNPs' content on the surface.

### 3. Conclusion

This work demonstrated the simple fabrication of complex 3D-printed parts with controlled characteristics, taking advantage of the selective reduction of silver precursors dispersed into a photocurable resin. Unlike other methods, where the AgNPs generation was accomplished in a post-processing step (e.g., thermally or light-induced), this work introduced an alternative strategy to achieve the resin photopolymerization and the photogeneration of AgNPs in the same printing process. The 3D printing strategy proposed here could be a different option for the conventional multi-material approach since the whole material is fabricated using the same polymer resin, avoiding adhesion problems, thermal expansion, incompatibility, or other issues between different materials. Conversely, the results presented here were obtained by willfully adjusting the printing parameters during the printing process, enabling thus the selective photogeneration of silver nanoparticles during the same light-based 3D printing step. Furthermore, by carrying out a post-3D printing protocol consisting of an overnight washing procedure, the unreduced silver salts were removed without compromising the part's structural integrity. This washing procedure might avoid the uncontrolled generation of AgNPs over time, stabilizing materials properties and features. Finally, antimicrobial activity versus environmental

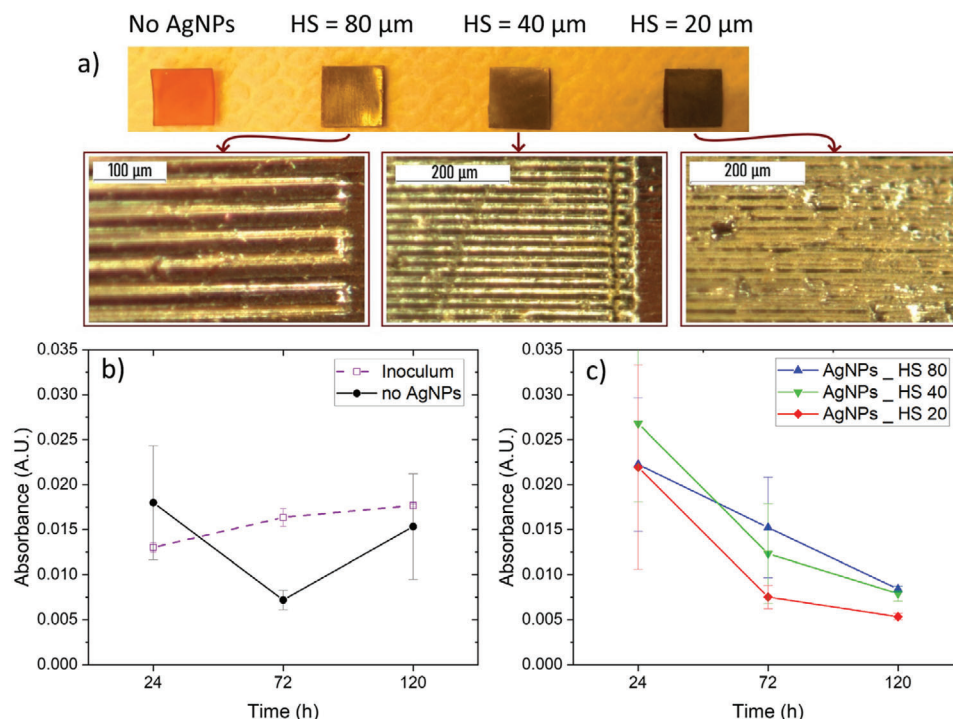


**Figure 5.** a) Pictures of the 3D-printed samples used for antibacterial tests showing the differences between the three hatch spacings (HS) of 80, 40, and 20  $\mu\text{m}$ . Results from UV-vis analysis: b) absorbance values over time for the liquid solution containing only bacteria and medium (inoculum) in a 1:100 ratio and the same solution with the presence of 3D printed samples without silver nanoparticles generation (no AgNPs). c) Absorbance values over time for the bacteria solution containing: (i) 3D printed samples with silver nanoparticles generated with hatch spacing of 80  $\mu\text{m}$  (AgNPs\_HS 80), (ii) 3D printed samples with silver nanoparticles generated with hatch spacing of 40  $\mu\text{m}$  (AgNPs\_HS 40), (iii) 3D printed samples with silver nanoparticles generated with hatch spacing of 20  $\mu\text{m}$  (AgNPs\_HS 20).

bacteria was demonstrated for silver-patterned 3D printed structures, with a time dependence in good agreement with the ion release-based antimicrobial mechanism attributed to the silver nanoparticles' photo-induced generation on the object surface. Such surface-engineered 3D-printed structures might be applied in areas where the control and track of bacterial growth are required.

## 4. Experimental Section

**Chemicals:** Poly(ethylene glycol) diacrylate (PEGDA575,  $M_w$  575 g  $\text{mol}^{-1}$ ) was used as a monomer for the photocurable formulation. Phenylbis (2,4,6-trimethyl benzoyl) phosphine oxide (BAPO) and 2-hydroxy-2-methyl-1-phenyl-propan-1-one (HMPP) were the photoinitiators. Silver Nitrate ( $\text{AgNO}_3$ ,  $\geq 99.0\%$ ) was employed as a silver precursor and acetonitrile (99.8%) solvent. Reactive Orange 16 (RO16,  $\geq 70\%$ ) was used as a dye in the formulation. All reagents were purchased from Merck and used as received.

**Preparation of the Photocurable Formulation Containing Silver Salt:** The printable formulation was prepared by adding 1 phr (per hundred of resins) of BAPO, 2 phr of HMPP, and 0.2 phr of RO in PEGDA575 and sonicated for 30 min using an ultrasonic tip (Branson SFX250).  $\text{AgNO}_3$  was dissolved into acetonitrile (0.786 g  $\text{mL}^{-1}$ ) and sonicated for 5 min. Then, this solution was added to the PEGDA-based formulation to reach an  $\text{AgNO}_3$  content of 15 wt%. This concentration was selected since it was found to present the best compromise between printability and viscosity.<sup>[27]</sup> Furthermore, a formulation without silver precursors was prepared as a reference.

**3D Printing and Silver Nanoparticles Generation:** A customized top-down stereolithography (SL) 3D printer (Microla Optoelectronics s.r.l.) was used to process the photocurable resins. The SL printer is equipped with a laser emitting at 405 nm, with an average beam diameter of 80  $\mu\text{m}$  and maximum laser nominal output power of 120 mW. The printer build area is 170  $\times$  200  $\text{mm}^2$ , and the object layer thickness can be tailored from 25 to 200  $\mu\text{m}$ . 3D printing was performed in the air atmosphere. After the 3D printing and AgNPs generation steps, the parts were rinsed in 2-propanol and immersed in deionized water overnight (about 16 h), followed by a slow and controlled drying step at room temperature for removing the unreacted components (monomer, photoinitiator, dye, and silver salt) without damaging the samples. Finally, each side of the samples (washed and dried) was subjected to a UV post-curing treatment for 15 minutes using a UV lamp (Hamamatsu Lightning Cure LC8) at 10% power. SolidWorks CAD software was used to design the CAD files and convert them to STL-type files.

**Sample Characterization—FT-IR Spectroscopy:** The spectrometer used was a Nicolet iS50 FT-IR from Thermo Fisher Scientific, Milano, Italy, equipped with an attenuated total reflection (ATR) accessory (Smart iTX, Thermo Fisher Scientific, Milano, Italy). This instrument was used to monitor, in real-time, the evolution of acrylate functional groups during visible irradiation and calculate the final acrylate conversion on the 3D-printed samples. The spectra were recorded with a resolution of 4  $\text{cm}^{-1}$  in the wavelength range between 650 and 4000  $\text{cm}^{-1}$  averaging 16 scans for each spectrum. For the real-time measurements, a 50  $\mu\text{m}$  thick film of the specific formulation was applied onto a silicon wafer and irradiated during the test in transmission mode with a portable laser emitting at 405 nm adapted to the spectrometer (nominal output light intensity of 5  $\text{mW cm}^{-2}$ ). The conversion of acrylate double bonds was monitored by following the band decrease related to the C=C bond at 1640  $\text{cm}^{-1}$ . The



spectra were normalized using the area of the carbonyl ester band at 1720  $\text{cm}^{-1}$ .

**Sample Characterization—Ultraviolet–Visible Spectroscopy:** UV–vis measurements were carried out using a double-beam Lambda 40 spectrophotometer (PerkinElmer Italia, Milano, Italy) in the range between 300 and 800 nm and at a scan rate of 480  $\text{nm min}^{-1}$ . The tests on solid samples were performed on 50  $\mu\text{m}$  thick polymerized samples produced on a laboratory glass slide using the customized SL-3D printer.

**Sample Characterization—Insoluble Fraction:** The polymerized samples' insoluble fraction (gel content) was determined following the standard test method ASTM D2765–84. The specimens were kept in a metal net, precisely weighed, and subsequently immersed in chloroform ( $\text{CHCl}_3$ ) for 24 h at room temperature to dissolve the non-crosslinked products. Then, the samples were dried overnight at 80  $^\circ\text{C}$ , and the insoluble fraction percentage was determined as the weight change before and after the solvent extraction.

**Sample Characterization—Field Emission Scanning Electron Microscopy (FESEM):** The morphological characterizations were performed on the sample's surface and cross-section using a field emission scanning electron microscope (FESEM, Zeiss Supra 40). The cross-section images were collected on samples fractured in liquid nitrogen.

**Sample Characterization—X-Ray Photoelectron Spectroscopy (XPS):** A PHI 5000 Versaprobe scanning X-ray photoelectron spectrometer (monochromatic Al K- $\alpha$  X-ray source with 1486.6 eV energy, 15 kV voltage, and 1 mA anode current) was used to investigate the surface chemical characteristics of the silver-based samples. A spot size of 100  $\mu\text{m}$  was used to collect the photoelectron signal for both the high resolution (HR) and the survey spectra. Different pass energy values were employed: 187.85 eV for survey spectra and 23.5 eV for HR peaks. All samples were analyzed with a combined electron and argon (Ar) ion gun neutralizer system to reduce the charging effect during the measurements. All core level peak energies were referenced to C 1s peak at 284.5 eV, and the background contribution in HR scans was subtracted using a Shirley function.<sup>[78]</sup> Spectra were analyzed using Multipak 9.6 dedicated software. Depth profile was performed in an alternate mode with sputtering cycles of 1 min each, through ionized argon ( $\text{Ar}^+$ ) flux at 2 kV accelerating voltage.

**Assessment of Antimicrobial Activity:** The antimicrobial/antibacterial effect of the photogenerated AgNPs was assessed in environmental bacteria presence (seawater bacteria). Squared samples with an area of 10  $\times$  10  $\text{mm}^2$  and thickness of 1 mm were printed using the customized SL printer. The silver ions reduction into silver nanoparticles was induced following a horizontal linear pattern, obtaining squared antibiotic tabs on their upper surface. The distance between the pattern lines rich in AgNPs (hatch spacing) was modified to observe different silver nanoparticles densities per unit area on the bacteria activity. Three different types of samples containing silver nanoparticles were prepared for the antibacterial tests: i) lines with hatch spacing of 0.08 mm; ii) lines with hatch spacing of 0.04 mm, and iii) lines with hatch spacing equal to 0.02 mm. Moreover, three samples were prepared from  $\text{AgNO}_3$  resin without AgNPs generation. Before the antibacterial tests, each specimen was washed in deionized water for 12 h and subjected to 15 minutes of UV postcuring treatment. With the main aim to demonstrate the antimicrobial activity due to the presence of silver nanoparticles into 3D printed samples and, at the same time, the repeatability of obtained results, three different repetitions were prepared for each sample containing silver nanoparticles and for reference material, 3D-printed without AgNPs generation.

Environmental microorganisms were added to a medium solution in a 1:100 ratio. The medium solution contained all compounds suitable to ensure bacterial proliferation, such as sodium acetate (1 g  $\text{L}^{-1}$ ), sodium dihydrogen phosphate ( $\text{NaH}_2\text{PO}_4$  at 2.45 g  $\text{L}^{-1}$ ), disodium hydrogen phosphate ( $\text{Na}_2\text{HPO}_4$  at 4.28 g  $\text{L}^{-1}$ ), potassium chloride (KCl at 0.13 g  $\text{L}^{-1}$ ), ammonium chloride ( $\text{NH}_4\text{Cl}$  at 0.31 g  $\text{L}^{-1}$ ). Each antimicrobial/antibacterial squared tab was immersed in 10 mL of such bacterial suspension. The bacteria viability was assessed by analyzing the liquid bacterial suspension using UV–vis spectroscopy (Lambda 40 instrument spectrophotometer—PerkinElmer, with an absorbance wavelength of 600 nm) after 24, 72, and 120 h of incubation at room temperature. Absorbance values were acquired, averaged, and finally plotted to compare

the different samples. The use of spectroscopy for evaluating the viability and growth of microorganisms like bacteria is reported elsewhere.<sup>[79,80]</sup> Spectroscopy was also performed on three samples with no 3D-printed part containing silver to be used as a reference.

## Supporting Information

Supporting Information is available from the Wiley Online Library or from the author.

## Acknowledgements

The present work was developed in the framework of DEFLeCT project funded by Regione Piemonte POR-FESR 2014–2020.

Open Access Funding provided by Politecnico di Torino within the CRUI-CARE Agreement.

## Conflict of Interest

The authors declare no conflict of interest.

## Data Availability Statement

The data that supports the findings of this study are available in the Supporting Information of this article.

## Keywords

3D printing, additive manufacturing, antibacterial properties, micropatterning, smart materials

Received: August 12, 2021  
Revised: September 21, 2021  
Published online: October 15, 2021

- [1] R. Tino, R. Moore, S. Antoline, P. Ravi, N. Wake, C. N. Ionita, J. M. Morris, S. J. Decker, A. Sheikh, F. J. Rybicki, L. L. Chepelev, *3D Print. Med.* **2020**, 6, 11.
- [2] Cavallo L., Marcianò A., Cicciù M., Oteri G., *Prosthesis* **2020**, 2, 46.
- [3] V. Krishnadoss, B. Kanjilal, A. Hesketh, C. Miller, A. Mugweru, M. Akbar, A. Khademhosseini, J. Leijten, I. Noshadi, *Chem. Eng. J.* **2021**, 409, 128213.
- [4] H. Kim, F. Torres, D. Villagran, C. Stewart, Y. Lin, T. L. B. Tseng, *Macromol. Mater. Eng.* **2017**, 302, 1700229.
- [5] T. D. Ngo, A. Kashani, G. Imbalzano, K. T. Q. Nguyen, D. Hui, *Composites, Part B* **2018**, 143, 172.
- [6] X. Wang, M. Jiang, Z. Zhou, J. Gou, D. Hui, *Composites, Part B* **2017**, 110, 442.
- [7] S. C. Ligon, R. Liska, J. Stampfl, M. Gurr, R. Mülhaupt, *Chem. Rev.* **2017**, 117, 10212.
- [8] R. L. Truby, J. A. Lewis, *Nature* **2016**, 540, 371.
- [9] L. Li, F. Yu, J. Shi, S. Shen, H. Teng, J. Yang, X. Wang, Q. Jiang, *Sci. Rep.* **2017**, 7, 9416.
- [10] Y. Liu, Q. Hamid, J. Snyder, C. Wang, S. Wei, *Rapid Prototyping J.* **2016**, 22, 947.
- [11] N. P. Macdonald, J. M. Cabot, P. Smejkal, R. M. Guijt, B. Paull, M. C. Bredmore, *Anal. Chem.* **2017**, 89, 3858.
- [12] G. Gonzalez, D. Baruffaldi, C. Martinengo, A. Angelini, A. Chiappone, I. Roppolo, F. C. Pirri, F. Frascella, *Nanomaterials* **2020**, 10, 1788.
- [13] R. D. Farahani, M. Dubé, D. Theriault, *Adv. Mater.* **2016**, 28, 5794.

- [14] V. Bertana, G. Scordo, M. Parmeggiani, L. Scaltrito, S. Ferrero, M. G. Gomez, M. Cocuzza, D. Vurro, P. D'Angelo, S. Iannotta, C. F. Pirri, S. L. Marasso, *Sci. Rep.* **2020**, *10*, 13335.
- [15] G. Scordo, V. Bertana, L. Scaltrito, S. Ferrero, M. Cocuzza, S. L. Marasso, S. Romano, R. Sesana, F. Catania, C. F. Pirri, *Mater. Today Commun.* **2019**, *19*, 12.
- [16] F. Wang, Y. Chong, F. K. Wang, C. He, J. *Appl. Polym. Sci.* **2017**, *134*, 1.
- [17] G. Gonzalez, A. Chiappone, I. Roppolo, E. Fantino, V. Bertana, F. Perucci, L. Scaltrito, F. Pirri, M. Sangermano, *Polymer* **2017**, *109*, 246.
- [18] Y.-L. Cheng, H.-L. Kao, in *Light Manip. Org. Mater. Devices II SPIE*, **2015**, vol. 9564, p. 95640K.
- [19] V. C. F. Li, X. Kuang, A. Mulyadi, C. M. Hamel, Y. Deng, H. J. Qi, *Cellulose* **2019**, *26*, 3973.
- [20] Z. Weng, Y. Zhou, W. Lin, T. Senthil, L. Wu, *Composites, Part A* **2016**, *88*, 234.
- [21] Z. Chen, Z. Li, J. Li, C. Liu, C. Lao, Y. Fu, C. Liu, Y. Li, P. Wang, Y. He, *J. Eur. Ceram. Soc.* **2019**, *39*, 661.
- [22] Z. Li, H. Chen, C. Wang, L. Chen, J. Liu, R. Liu, *J. Polym. Sci., Part A: Polym. Chem.* **2018**, *56*, 994.
- [23] S. Y. Song, M. S. Park, D. Lee, J. W. Lee, J. S. Yun, *Mater. Des.* **2019**, *180*, 107960.
- [24] E. Blasco, J. Müller, P. Müller, V. Trouillet, M. Schön, T. Scherer, C. Barner-Kowollik, M. Wegener, *Adv. Mater.* **2016**, *28*, 3592.
- [25] Q. Mu, L. Wang, C. K. Dunn, X. Kuang, F. Duan, Z. Zhang, H. J. Qi, T. Wang, *Addit. Manuf.* **2017**, *18*, 74.
- [26] D. Lin, S. Jin, F. Zhang, C. Wang, Y. Wang, C. Zhou, G. J. Cheng, *Nanotechnology* **2015**, *26*, 434003.
- [27] E. Fantino, A. Chiappone, I. Roppolo, D. Manfredi, R. Bongiovanni, C. F. Pirri, F. Calignano, *Adv. Mater.* **2016**, *28*, 3712.
- [28] J. A. Weisman, J. Nicholson, K. Tappa, U. Jammalamadaka, C. Wilson, D. Mills, *Int. J. Nanomed.* **2015**, *10*, 357.
- [29] J. M. Zuniga, *Appl. Sci.* **2018**, *8*, 1651.
- [30] G. D. Bixler, B. Bhushan, *Philos. Trans. R. Soc., A* **2012**, *370*, 2381.
- [31] M. Vivero-Lopez, X. Xu, A. Muras, A. Otero, A. Concheiro, S. Gaisford, A. W. Basit, C. Alvarez-Lorenzo, A. Goyanes, *Mater. Sci. Eng., C* **2021**, *119*, 111606.
- [32] X. Y. Tai, A. Zhakeyev, H. Wang, K. Jiao, H. Zhang, J. Xuan, *Fuel Cells* **2019**, *19*, 636.
- [33] A. Fotiadou, I. Papagiannopoulos-Miaoulis, *Front. Energy Res.* **2019**, *7*, 1.
- [34] A. Siria, M. L. Bocquet, L. Bocquet, *Nat. Rev. Chem.* **2017**, *1*, 0091.
- [35] Z. Jia, B. Wang, S. Song, Y. Fan, *Renewable Sustainable Energy Rev.* **2014**, *31*, 91.
- [36] N. Khan, A. Kalair, N. Abas, A. Haider, *Renewable Sustainable Energy Rev.* **2017**, *72*, 590.
- [37] S. H. Yang, J. W. Ringsberg, E. Johnson, Z. Hu, *Appl. Ocean Res.* **2017**, *65*, 166.
- [38] E. Bar-Zeev, F. Perreault, A. P. Straub, M. Elimelech, *Environ. Sci. Technol.* **2015**, *49*, 13050.
- [39] S. S. Bucs, R. Valladares Linares, J. S. Vrouwenvelder, C. Picioreanu, *Water Res.* **2016**, *106*, 86.
- [40] Z. Li, C. Wang, W. Qiu, R. Liu, *Photochem. Photobiol.* **2019**, *95*, 1219.
- [41] C. Garcia, A. Gallardo, D. López, C. Elvira, A. Azahti, E. Lopez-Martinez, A. L. Cortajarena, C. M. González-Henríquez, M. A. Sarabia-Vallejos, J. Rodríguez-Hernández, *ACS Appl. Bio Mater.* **2018**, *1*, 1337.
- [42] C. M. González-Henríquez, M. A. Sarabia-Vallejos, J. R. Hernandez, *Int. J. Mol. Sci.* **2019**, *20*, 1210.
- [43] W. Ahmed, S. Siraj, A. H. Al-Marzouqi, *Polymer* **2021**, *13*, 1523.
- [44] H. Qiu, Z. Si, Y. Luo, P. Feng, X. Wu, W. Hou, Y. Zhu, M. B. Chan-Park, L. Xu, D. Huang, *Front. Bioeng. Biotechnol.* **2020**, *8*, 910.
- [45] J. Yue, P. Zhao, J. Y. Gerasimov, M. van de Lagemaat, A. Grotenhuis, M. Rustema-Abbing, H. C. van der Mei, H. J. Busscher, A. Herrmann, Y. Ren, *Adv. Funct. Mater.* **2015**, *25*, 6756.
- [46] J. C. Wang, H. Zheng, M. W. Chang, Z. Ahmad, J. S. Li, *Sci. Rep.* **2017**, *7*, 1.
- [47] Z. Zhou, Q. Yao, L. Li, X. Zhang, B. Wei, L. Yuan, L. Wang, *Med. Sci. Monit.* **2018**, *24*, 6934.
- [48] L. Bonilla-Gameros, P. Chevallier, A. Sarkissian, D. Mantovani, *Nanomed.: Nanotechnol., Biol. Med.* **2020**, *24*, 102142.
- [49] A. Abbas, G. Yasamin, G. Ahmad, H. Bahram, D. Samira, N. Moham-madreza, S. Hashem, *J. Nanomater.* **2015**, *53*, 8.
- [50] C. F. Carlborg, T. Haraldsson, K. Oberg, M. Malkoch, W. Van der Wi-jngaart, *Lab Chip* **2011**, *11*, 3136.
- [51] C. Liao, Y. Li, S. C. Tjong, *Int. J. Mol. Sci.* **2019**, *20*, 449.
- [52] S. Agnihotri, S. Mukherji, S. Mukherji, *Nanoscale* **2013**, *5*, 7328.
- [53] I. Francolini, C. Vuotto, A. Piozzi, G. Donelli, *APMIS* **2017**, *125*, 392.
- [54] M. Akter, M. T. Sikder, M. M. Rahman, A. K. M. A. Ullah, K. F. B. Hossain, S. Banik, T. Hosokawa, T. Saito, M. Kurasaki, *J. Adv. Res.* **2018**, *9*, 1.
- [55] M. Kawish, F. Ullah, H. S. Ali, S. Saifullah, I. Ali, J. Rehman, M. Im-ran, *Metal Nanoparticles for Drug Delivery and Diagnostic Applications*, Elsevier Inc., Amsterdam, **2020**.
- [56] N. Mobarki, B. Almerabi, A. Hattan, *Int. J. Med. Dev. Countries* **2019**, *40*, 561.
- [57] P. Maróti, B. Kocsis, A. Ferencz, M. Nyitrai, D. Lőrinczy, *J. Therm. Anal. Calorim.* **2020**, *139*, 367.
- [58] A. J. Lopes, I. H. Lee, E. Macdonald, R. Quintana, R. Wicker, *J. Mater. Process. Technol.* **2014**, *214*, 1935.
- [59] E. Fantino, A. Chiappone, F. Calignano, M. Fontana, F. Pirri, I. Rop-polo, *Materials* **2016**, *9*, 589.
- [60] H. Jin, H. Guo, X. Gao, R. Gui, *Sens. Actuators, B* **2018**, *277*, 14.
- [61] E. T. Tenório-Neto, M. R. Guilherme, M. E. G. Winkler, L. Cardozo-Filho, S. C. Beneti, A. F. Rubira, M. H. Kunita, *Mater. Lett.* **2015**, *159*, 118.
- [62] L. Deng, Y. Deng, K. Xie, *Colloids Surf., B* **2017**, *160*, 483.
- [63] S. Radhakrishnan, S. Nagarajan, H. Belaid, C. Farha, I. Iatsunskiy, E. Coy, L. Soussan, V. Huon, J. Bares, K. Belkacemi, C. Teyssier, S. Balme, P. Miele, D. Cornu, *Mater. Sci. Eng., C* **2021**, *118*, 111525.
- [64] Y. Zhang, D. Zhai, M. Xu, Q. Yao, H. Zhu, J. Chang, C. Wu, *Biofabri-cation* **2017**, *9*, 025037.
- [65] S. Chen, J. Yang, Y. G. Jia, B. Lu, L. Ren, *Materials* **2018**, *11*, 2444.
- [66] İ. Aktitiz, R. Varol, N. Akkurt, M. F. Saraç, *Polym. Test.* **2020**, *90*, 106724.
- [67] F. Li, N. P. Macdonald, R. M. Guijt, M. C. Breadmore, *Lab Chip* **2019**, *19*, 35.
- [68] A. Badev, Y. Abouliatim, T. Chartier, L. Lecamp, P. Lebaudy, C. Chaput, C. Delage, *J. Photochem. Photobiol., A* **2011**, *222*, 117.
- [69] K. Taki, Y. Watanabe, H. Ito, M. Ohshima, *Macromolecules* **2014**, *47*, 1906.
- [70] V. Jančovičová, M. Mikula, B. Havlínová, Z. Jakubíková, *Prog. Org. Coat.* **2013**, *76*, 432.
- [71] I. Roppolo, M. Castellino, K. Bejtka, G. Rizza, D. Perrone, P. E. Coulon, A. Chiappone, K. Rajan, S. Bocchini, C. Ricciardi, C. F. Pirri, A. Chio-lerio, *J. Phys. Chem. C* **2017**, *121*, 14285.
- [72] A. Barbieri, G. Accorsi, N. Armaroli, *Chem. Commun.* **2008**, 2185.
- [73] K. Hashiguchi, M. Kamiya, H. Tanimoto, *Mater. Trans.* **2018**, *59*, 648.
- [74] B. Steyrer, P. Neubauer, R. Liska, J. Stampfl, *Materials* **2017**, *10*, 1445.
- [75] M. Milošević, M. Radoičić, Z. Šaponjić, T. Nunney, C. Deeks, V. Lazić, M. Mitrić, T. Radetić, M. Radetić, *Cellulose* **2014**, *21*, 3781.
- [76] T. Yuranova, A. G. Rincon, A. Bozzi, S. Parra, C. Pulgarin, P. Albers, J. Kiwi, *J. Photochem. Photobiol., A Chem.* **2003**, *161*, 27.
- [77] U. Simon, S. Dimartino, *J. Chromatogr. A* **2019**, *1587*, 119.
- [78] D. A. Shirley, *Phys. Rev. B* **1972**, *5*, 4709.
- [79] C. E. Alupoaei, L. H. García-Rubio, *Biotechnol. Bioeng.* **2004**, *86*, 163.
- [80] R. Davis, A. Deering, Y. Burgula, L. J. Mauer, B. L. Reuhs, *J. Appl. Microbiol.* **2012**, *112*, 743.